

arXiv:2411.06442v1 [cs.CV] 10 Nov 2024

Local Implicit Wavelet Transformer for Arbitrary-Scale Super-Resolution

Minghong Duan^{1,2}

22111010025@m.fudan.edu.cn

Linhao Qu^{1,2}

lhqu20@fudan.edu.cn

Shaolei Liu^{1,2}

19111010029@m.fudan.edu.cn

Manning Wang^{1,2*}

mnwang@fudan.edu.cn

¹ Digital Medical Research Center
Fudan University
Shanghai, China² Shanghai Key Lab of Medical
Image Computing and Computer
Assisted Intervention

Abstract

Implicit neural representations have recently demonstrated promising potential in arbitrary-scale Super-Resolution (SR) of images. Most existing methods predict the pixel in the SR image based on the queried coordinate and ensemble nearby features, overlooking the importance of incorporating high-frequency prior information in images, which results in limited performance in reconstructing high-frequency texture details in images. To address this issue, we propose the Local Implicit Wavelet Transformer (LIWT) to enhance the restoration of high-frequency texture details. Specifically, we decompose the features extracted by an encoder into four sub-bands containing different frequency information using Discrete Wavelet Transform (DWT). We then introduce the Wavelet Enhanced Residual Module (WERM) to transform these four sub-bands into high-frequency priors, followed by utilizing the Wavelet Mutual Projected Fusion (WMPF) and the Wavelet-aware Implicit Attention (WIA) to fully exploit the high-frequency prior information for recovering high-frequency details in images. We conducted extensive experiments on benchmark datasets to validate the effectiveness of LIWT. Both qualitative and quantitative results demonstrate that LIWT achieves promising performance in arbitrary-scale SR tasks, outperforming other state-of-the-art methods. The code is available at <https://github.com/dmhdhmh/LIWT>.

1 Introduction

Single Image Super-Resolution (SISR) refers to the process of recovering a high-resolution (HR) image from a single low-resolution (LR) image and has been widely applied across various fields [8, 10, 24, 26, 25]. Most existing SISR models comprise a deep neural network (DNN) with an upsampling module like learnable deconvolutions or pixel shuffling [8, 25] and can only deal with integer scaling factors, and these models necessitate retraining when encountering new scaling factors. Recent work has achieved arbitrary-scale super-resolution

*Corresponding Author.

© 2024. The copyright of this document resides with its authors.

It may be distributed unchanged freely in print or electronic forms.

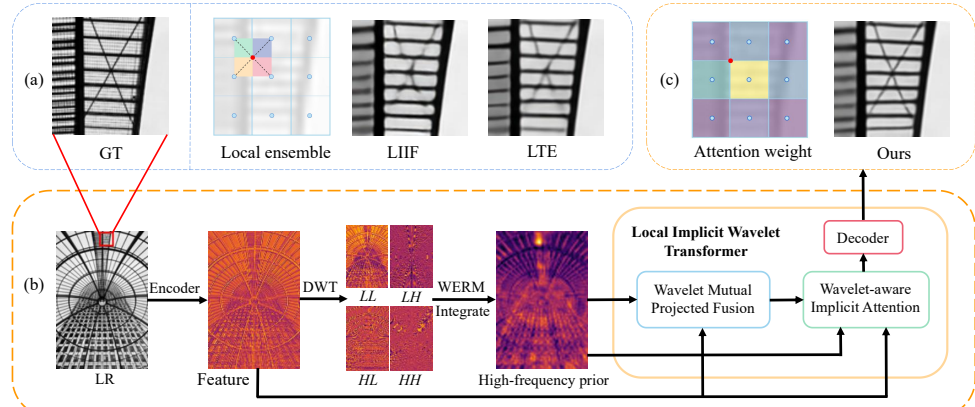


Figure 1: Motivation and effectiveness of our method. (a) LIIF [5] and LTE [16] have difficulty reconstructing high-frequency details using the local ensemble technique. (b) LIWT introduces the high-frequency prior via DWT. (c) LIWT can reconstruct high-frequency details using attention weight based on the high-frequency prior.

(SR) by replacing the upsampling layer typically used in previous methods with a local implicit image function and has demonstrated exemplary performance [5, 16]. These methods based on local implicit functions first extract features from LR images through a DNN-based encoder and then employ multi-layer perceptrons (MLPs) to map the 2D query coordinates of the HR image and the aggregated representation of the corresponding local region features (called latent code) to RGB values. There are two limitations to these existing methods. Firstly, the coordinate-based local ensemble technique [5, 16] used for querying RGB values fails to consider the relevance of features within local regions. Ensemble weights are typically computed based on the rectangular area between the query point and each nearest point (Figure 1(a)). These weights are solely dependent on the positional relationship between the query point and its nearest coordinates of local features and do not account for the features themselves, thus limiting the reconstruction performance of the model. Secondly, only the four nearest latent codes to the query point are used when querying RGB values based on coordinates. We argue that the representational capacity of LR features directly obtained from the encoder is limited, especially in large-scale SR, which may lead to blurry results lacking texture details. Introducing high-frequency prior information of image features into the local implicit functions is therefore necessary.

Many existing methods have shown that high-frequency prior information obtained from discrete wavelet transform (DWT) can improve the performance of SR models based on deep learning [10, 28, 34]. However, the scale transformation rate of the DWT when applied to features or images is limited to powers of 2, and most DWT-based methods rely on this property for inverse transformation to achieve upsampling, thereby not achieving arbitrary-scale SR. To better restore high-frequency details while achieving arbitrary resolution upscaling, we propose the Local Implicit Wavelet Transformer (LIWT), which leverages cross-attention to exploit the high-frequency information obtained from DWT fully and accounts for the relevance of the features within a local region. As shown in Figure 1(b), LIWT consists of a Wavelet Mutual Projected Fusion (WMPF), a Wavelet-aware Implicit Attention (WIA), and a decoder. We first extract features from the LR image using an encoder and then decompose the features obtained into low-frequency components LL and high-frequency components LH , HL , and HH using DWT. To enhance LIWT's capability

to capture high-frequency details, we designed the Wavelet Enhancement Residual Module (WERM) to integrate the four components obtained by DWT and output features with high-frequency priors. Subsequently, we fuse the high-frequency priors with the features from the encoder using WMPF to assist in reconstruction. Then, we employed WIA to generate attention maps based on query coordinates and sample nearest-neighbor interpolated latent vectors from both the high-frequency prior features and the original features. By applying these attention maps to these feature embeddings, LIWT focuses more on high-frequency details in the image. Finally, the decoder utilizes attention feature embeddings to generate RGB values. As illustrated in Figure 1(c), employing attention weight based on high-frequency priors enables the reconstruction of high-frequency details.

The main contributions of our work are summarized as follows: (1) We introduce the Local Implicit Wavelet Transformer (LIWT), which integrates features obtained from DWT into local implicit image functions using the designed WERM and WIA to enhance performance; (2) We demonstrate that LIWT can be effectively integrated into different encoders to enhance performance, outperforming other arbitrary-scale SR methods; (3) We conduct a comprehensive analysis of LIWT. Extensive experimental results demonstrate that the proposed LIWT can produce superior or comparable results on benchmark datasets.

2 Related work

Single image super-resolution. SRCNN [7] pioneered the implementation of SISR using a convolutional neural network (CNN) in an end-to-end manner, subsequently leading to a series of methods that utilized other CNN modules designed to enhance SR performance further. Examples include methods employing residual modules such as EDSR [18] or dense connection modules such as RDN [33]. In addition, methods based on attention mechanisms [8, 9, 17, 27, 28, 29, 30, 31] have been introduced into SISR, including channel attention [8, 23, 32], self-attention [8, 17], and non-local attention [27, 29].

DWT based image super-resolution. DWT has been widely used in SISR due to its ability to express different frequency components [10, 11, 14, 28, 31, 34]. To leverage the high-frequency representation capability of DWT, WDRN [28] guides the feature extraction process to preserve high-frequency features in the wavelet domain, reconstructing HR images with more precise details; JWSGN [34] utilizes DWT to transform input features into the frequency domain and generate edge feature maps to correct high-frequency components, further recovering high-frequency details. Despite their impressive results, these SISR models require training different models for each upscaling factor, limiting their applicability.

Arbitrary-scale super-resolution. Several methods have been proposed to train a unified model capable of handling arbitrary upscaling factors [8, 9, 13, 16, 20, 29]. LIIF [8] employs an MLP as a local implicit function, which predicts the RGB values at any query coordinate by acquiring the HR image coordinates and the features around the coordinates. LTE [16] further introduces a local texture estimator that enriches the representation capability of local implicit functions by predicting Fourier information. Unlike the above methods, we introduce the high-frequency prior obtained from the wavelet transform into the local implicit function, further improving the recovery of high-frequency details.

3 Methodology

The overall framework of the proposed model, which integrates the encoder, the Wavelet Enhancement Residual Module (WERM), and the LIWT, is given in Figure 2(a). For a

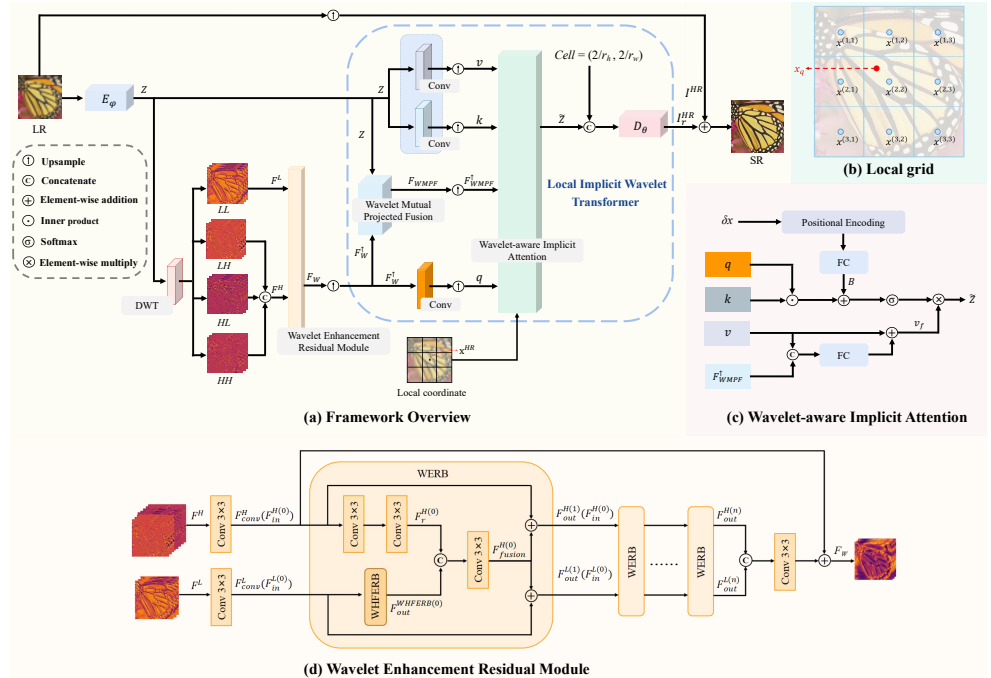


Figure 2: (a) Overview of the proposed framework. (b) Diagram of the local grid. (c) Structure of the WIA. (d) Structure of the WERM.

given LR image $I^{LR} \in R^{H \times W \times 3}$ at the 2D LR coordinates $x^{LR} \in \chi$ and any magnification $s = \{s_h, s_w\}$, the model outputs an HR image $I^{HR} \in R^{s_h H \times s_w W \times 3}$ at the 2D HR coordinates $x^{HR} \in \chi$, where χ is the 2D coordinate space used to express the continuous 2D image domain. First, we employ the encoder E_ϕ to extract features from the LR image, obtaining $Z \in R^{H \times W \times C}$. Subsequently, we decompose Z using discrete wavelet transform (DWT) into low-frequency component LL and high-frequency components LH , HL , and HH . The low-frequency component LL is denoted as F^L , while the high-frequency components LH , HL , and HH are concatenated along the channel axis and represented as F^H . We further process F^L and F^H using WERM to isolate high-frequency information, yielding enhanced texture features $F_W \in R^{H/2 \times W/2 \times C}$ as high-frequency priors. We perform bicubic upsampling of F_W to obtain $F_W^{\uparrow} \in R^{H \times W \times C}$ and input it with the feature Z and the 2D HR coordinate x^{HR} into the LIWT to generate the RGB values of the residual image $I_r^{HR} \in R^{s_h H \times s_w W \times 3}$. Finally, the residual image $I_r^{HR} \in R^{s_h H \times s_w W \times 3}$ is summed via element-wise addition with the bilinearly upsampled image $I_{\uparrow}^{HR} \in R^{s_h H \times s_w W \times 3}$ to generate the final predicted HR image I^{HR} . LIWT consists of the Wavelet Mutual Projected Fusion (WMPF), the Wavelet-aware Implicit Attention (WIA), and a decoder, collectively utilizing the high-frequency prior F_W to recover image details. We train the entire framework using the L1 loss and utilize the Haar wavelet transform to perform the DWT.

3.1 Wavelet Enhancement Residual Module

To extract more high-frequency information conducive to reconstruction from the different components obtained through DWT decomposition, we devised WERM to process F^L and F^H , which comprises several wavelet enhancement residual blocks (WERBs). As il-

lustrated in Figure 2(d), the input to the k th WERB is denoted as $F_{in}^{L(k)}$ and $F_{in}^{H(k)}$, and the output is denoted as $F_{out}^{L(k)}$ and $F_{out}^{H(k)}$. Initially, we preprocess F^L and F^H separately using a 3×3 convolutional layer to obtain F_{conv}^L and F_{conv}^H , which are then fed into the first WERB. We further designed a wavelet high-frequency enhancement residual block (WHFERB) to separate more sharp edge components from the smoothed surface of $F_{in}^{L(k)}$ and assist in reconstruction at each WERB. Figure 3 shows WHFERB consists of a Wavelet Local Feature Extraction (WLFE) branch and a Wavelet High-Frequency Enhancement (WHFE) branch. For the WLFE branch, we employ a 3×3 convolutional layer followed by a ReLU activation function to extract local features. For the WHFE branch, we employ a max-pooling layer to extract high-frequency information from the input features and use a 3×3 convolutional layer followed by a ReLU activation function to enhance the high-frequency features. Subsequently, we concatenate the outputs of the two branches and input them into a 1×1 convolutional layer for information fusion. We refine the high-frequency feature $F_{in}^{H(k)}$ through two consecutive 3×3 convolutional layers to obtain $F_r^{H(k)}$. Then, the outputs of the two branches are concatenated and input into a 3×3 convolutional layer for information fusion to obtain $F_{fusion}^{H(k)}$. To effectively utilize high-frequency information and maintain training stability, we introduce skip-connections to transmit the fused information $F_{fusion}^{H(k)}$ back to the two branches separately, allowing the frequency information of the two branches to complement each other. For the WERM containing n WERBs, we concatenate the outputs $F_{out}^{L(n)}$ and $F_{out}^{H(n)}$ of the n th WERB and fuse them using a 3×3 convolutional layer. We also introduce skip connections to add the fused result to F_{conv}^H to obtain the final high-frequency prior feature representation F_W . In this paper, we set n to 4.

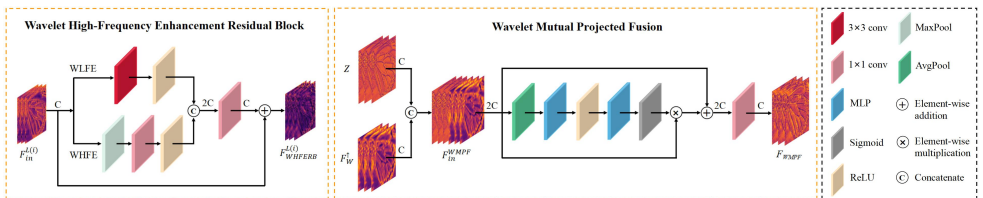


Figure 3: Structure of the WHFERB and the WMPF.

3.2 Local Implicit Wavelet Transformer

Overview. LIWT processes the high-frequency prior feature F_W and features Z from the encoder, and it outputs the RGB values of the corresponding residual image $I_r^{HR} \in R^{s_h H \times s_w W \times 3}$ based on the input 2D HR coordinates \mathbf{x}^{HR} . Figure 2(a) illustrates that it consists of the WMPF, the WIA, and a decoder D_θ parameterized by θ . To leverage the useful texture information from the high-frequency prior F_W , we perform bicubic upsampling on F_W to obtain F_W^\uparrow firstly, which has the same size as feature Z . Subsequently, we assign weight coefficients to each channel of F_W^\uparrow and feature Z and then fuse them to yield F_{WMPF} through WMPF. This operation aims to direct the LIWT to focus more on the high-frequency components in F_W^\uparrow that are beneficial for detail recovery. Simultaneously, we use convolutional layers to project F_W^\uparrow and derive the latent embedding corresponding to the query q . Additionally, using two separate convolutional layers, we project Z to obtain latent embeddings for key k and value v , respectively. WIA estimates the local latent embedding $\tilde{z} \in R^{9 \times C}$ for HR coordinates within

3×3 local grids based on the input q , k , v , and F_{WMPF} . Finally, D_θ utilizes these embeddings and the provided cell to predict the RGB values I_r^{HR} at the HR coordinates. The process of LIWT can be formalized as follows:

$$F_{WMPF} = WMPF(F_W^\uparrow, Z) \quad (1)$$

$$\tilde{z} = WIA(\delta\mathbf{x}, F_{WMPF}^\uparrow, q, k, v), \delta\mathbf{x} = \{x_q - x^{(i,j)}\}_{i \in \{1,2,3\}, j \in \{1,2,3\}} \quad (2)$$

$$I^r(x_q) = D_\theta(\tilde{z}, c) \quad (3)$$

where $x^{(i,j)}$ represents the LR coordinates within the local grids that are closest to the HR coordinates x_q , as shown in Figure 2(b). The query latent code $q \in R^{1 \times C}$ at the HR coordinate x_q is calculated by nearest neighbor interpolation, and the feature embeddings $F_{WMPF}^\uparrow \in R^{9 \times C}$, $k \in R^{9 \times C}$, and $v \in R^{9 \times C}$ are sampled at the local LR coordinate $\mathbf{x} = \{x^{i,j}\}_{i \in \{1,2,3\}, j \in \{1,2,3\}}$. $I^r(x_q)$ represents the predicted RGB value at the query coordinate x_q , $c = \{2/s_h H, 2/s_w W\}$ denotes the unit cell representing the height and width of pixels in the HR image, and D_θ is implemented as a five-layer MLP.

Wavelet Mutual Projected Fusion. LIWT utilizes WMPF to fuse the high-frequency details in F_W^\uparrow with the features Z from the encoder. As illustrated in Figure 3, WMPF first concatenates F_W^\uparrow and feature Z along the channel dimension to form the input F_{in}^{WMPF} . Subsequently, the entire input is represented through global average pooling, followed by learning the non-linear interactions within the concatenated features F_{in}^{WMPF} across channels using *FC-ReLU-FC* layers, where *FC* represents a fully connected layer. Finally, attention coefficients are obtained via a sigmoid activation function, which is then multiplied with the features F_{in}^{WMPF} at the channel level, enabling effective focus on the high-frequency components and contextual information of the features. Additionally, skip-connections are introduced to maintain training stability, and the fused features F_{WMPF} are outputted through a 1×1 convolutional layer.

Wavelet-aware Implicit Attention. As shown in Figure 2(c), LIWT utilizes WIA to perform cross-attention on the local grid, generating local latent embeddings $\tilde{z} \in R^{9 \times C}$ for each HR coordinate. To effectively utilize the fused features F_{WMPF} in the attention mechanism and avoid generating incorrect textures, we further fuse F_{WMPF}^\uparrow and value v to obtain v_f :

$$v_f = FC\left(\text{Concat}\left(v, F_{WMPF}^\uparrow\right)\right) + v \quad (4)$$

We define $q \in R^{1 \times C}$, $k \in R^{9 \times C}$, and $v \in R^{9 \times C}$ on the local grid as sets $q = \{q_\tau \mid \tau = 1, 2, \dots, H\}$, $k = \{k_\tau^r \mid r = 1, 2, \dots, 9, \tau = 1, 2, \dots, H\}$, and $v_f = \{v_\tau^r \mid r = 1, 2, \dots, 9, \tau = 1, 2, \dots, H\}$, where r represents the latent code index on local grid, H represents the number of attention heads, and we set H to 8. WIA first calculates the inner product of q and k , then adds the relative position deviation B to the calculation result to obtain the attention matrix. Subsequently, the attention matrix is normalized through Softmax operation to generate a local attention map. Finally, WIA performs element-wise multiplication on v_f and the local attention map and concatenates the operation results of different attention heads to obtain \tilde{z} :

$$\tilde{z} = \text{Concat}\left(\left\{\frac{\exp\left(\frac{q_\tau^r(k_\tau^r)^\top}{\sqrt{C/H}} + B\right)}{\sum_{r=1}^9 \exp\left(\frac{q_\tau^r(k_\tau^r)^\top}{\sqrt{C/H}} + B\right)} \times v_\tau^r\right\}_{\tau=1,2,\dots,H}\right) \quad (5)$$

$$B = FC(\gamma(\delta \mathbf{x})), \gamma(\delta \mathbf{x}) = [\sin(2^0 \delta \mathbf{x}), \cos(2^0 \delta \mathbf{x}), \dots, \sin(2^{L-1} \delta \mathbf{x}), \cos(2^{L-1} \delta \mathbf{x})] \quad (6)$$

where C represents the dimension of the latent embedding, γ is the position encoding function, and L is the encoding dimension hyperparameter and is set to 10.

Backbone	Methods	$\times 2$	$\times 3$	$\times 4$	$\times 6$	$\times 12$	$\times 18$	$\times 24$	$\times 30$
-	Bicubic	31.01	28.22	26.66	24.82	22.27	21	20.19	19.59
EDSR [15]	EDSR-baseline [15]	34.55	30.9	28.94	-	-	-	-	-
	EDSR-Meta-SR [15]	34.64	30.93	28.92	26.61	23.55	22.03	21.06	20.37
	EDSR-LIIF [15]	34.67	30.96	29.00	26.75	23.71	22.17	21.18	20.48
	EDSR-UltraSR [15]	34.69	31.02	29.05	26.81	23.75	22.21	21.21	20.51
	EDSR-IPE [15]	34.72	31.01	29.04	26.79	23.75	22.21	21.22	20.51
	EDSR-LTE [15]	34.72	31.02	29.04	26.81	23.78	22.23	21.24	20.53
	EDSR-LIWT(ours)	34.79	31.12	29.15	26.91	23.86	22.31	21.30	20.60
RDN [15]	RDN-baseline [15]	34.94	31.22	29.19	-	-	-	-	-
	RDN-Meta-SR [15]	35.00	31.27	29.25	26.88	23.73	22.18	21.17	20.47
	RDN-LIIF [15]	34.99	31.26	29.27	26.99	23.89	22.34	21.31	20.59
	RDN-UltraSR [15]	35.00	31.30	29.32	27.03	23.73	22.36	21.33	20.61
	RDN-IPE [15]	35.04	31.32	29.32	27.04	23.93	22.38	21.34	20.63
	RDN-LTE [15]	35.04	31.32	29.33	27.04	23.95	22.40	21.36	20.64
	RDN-LIWT(ours)	35.07	31.36	29.39	27.11	24.03	22.47	21.43	20.70
SwinIR [15]	SwinIR-baseline [15]	34.94	31.22	29.19	-	-	-	-	-
	SwinIR-Meta-SR [15]	35.15	31.40	29.33	26.94	23.80	22.26	21.26	20.54
	SwinIR-LIIF [15]	35.17	31.46	29.46	27.15	24.02	22.43	21.40	20.67
	SwinIR-LTE [15]	35.24	31.50	29.51	27.20	24.09	22.50	21.47	20.73
	SwinIR-LIWT(ours)	35.25	31.53	29.55	27.25	24.15	22.56	21.52	20.77

Table 1: Quantitative comparison on the DIV2K validation set [15], with the best and second best results highlighted in red and blue, respectively.

4 Experimental Results

4.1 Experimental Setup

Dataset. Following [8, 16], we train our model on the training set of the DIV2K dataset [15], which comprises 800 images with a resolution of 2K. We evaluate the performance on the DIV2K validation dataset and benchmark datasets, including Set5 [1], Set14 [31], B100 [21], and Urban100 [14]. Consistent with previous SR methods based on implicit neural representation [8, 13, 16, 70, 29], we employed PSNR as the evaluation metric. We also provide SSIM and LPIPS evaluation metrics in the appendix.

Curriculum Learning and Training details. Consistent with prior work [4, 16], we employed EDSR [15], RDN [15], and SwinIR [15] without upsampling modules to serve as encoders. For the synthesis of training data in each batch, we cropped patches of size $48s \times 48s$ from each HR image, then downsampled them using bicubic interpolation to produce LR images of size 48×48 as inputs to the model. Subsequently, we sampled 48^2 pixels from the corresponding cropped patches to form RGB-coordinate pairs as ground truth. To enhance the model’s ability to recover high-frequency details in large-scale SR, we proposed a curriculum learning training strategy. We trained the model for 1000 epochs. Within the first 250 epochs, we sampled the upsampling factor s from a uniform distribution $U(1, 4)$. In the range of epochs from 250 to 500, we sampled the upsampling factor s from a uniform distribution $U(1, 6)$. In the range of epochs from 500 to 1000, we sampled the upsampling factor s from a uniform distribution $U(1, 8)$. By gradually expanding the range of scale factor sampling during training, the model can progressively learn how to handle large scaling factors. We set the batch size to 32 and utilized the Adam optimizer. The learning rate was initially set to $1e-4$ and decayed by a factor of 0.5 every 200 epochs. Please refer to the appendix for our analysis of the training strategy.

Methods	Set5 [■]						Set14 [■]						B100 [■]						Urban100 [■]					
	$\times 2$	$\times 3$	$\times 4$	$\times 6$	$\times 8$	$\times 12$	$\times 2$	$\times 3$	$\times 4$	$\times 6$	$\times 8$	$\times 12$	$\times 2$	$\times 3$	$\times 4$	$\times 6$	$\times 8$	$\times 12$	$\times 2$	$\times 3$	$\times 4$	$\times 6$	$\times 8$	$\times 12$
RDN [■]	38.24	34.71	32.47	-	-	-	34.01	30.57	28.81	-	-	-	32.34	29.26	27.72	-	-	-	32.89	28.80	26.61	-	-	-
RDN-Meta-SR [■]	38.22	34.63	32.38	29.04	26.99	24.68	33.98	30.54	28.78	26.51	24.97	23.17	32.33	29.26	27.71	25.90	24.83	23.47	32.92	28.82	26.65	23.99	22.59	21.00
RDN-LIIF [■]	38.17	34.68	32.50	29.15	27.14	24.86	33.97	30.53	28.80	26.64	25.15	23.24	32.32	29.26	27.74	25.98	24.91	23.57	32.87	28.82	26.68	24.20	22.79	21.15
RDN-UltraSR [■]	38.21	34.67	32.49	29.33	27.24	24.81	33.97	30.59	28.86	26.69	25.25	23.32	32.35	29.29	27.77	26.01	24.96	23.59	32.97	28.82	26.78	24.30	22.87	21.20
RDN-IP-E [■]	38.11	34.68	32.51	29.25	27.22	-	33.94	30.47	28.75	26.56	25.09	-	32.31	29.28	27.76	26.00	24.93	-	32.97	28.82	26.76	24.26	22.87	-
RDN-LTE [■]	38.23	34.72	32.61	29.32	27.26	24.79	34.09	30.58	28.86	26.71	25.16	23.31	32.36	29.30	27.77	26.01	24.95	23.60	33.04	28.97	26.81	24.24	22.88	21.32
RDN-LIWT (ours) [■]	38.26	34.73	32.63	29.45	27.38	25.00	34.09	30.59	28.87	26.73	25.16	23.30	32.36	29.30	27.77	26.01	24.95	23.65	33.05	28.97	26.81	24.24	22.87	21.33
SwinIR [■]	38.35	34.89	32.72	-	-	-	34.14	30.77	28.94	-	-	-	32.44	29.37	27.83	-	-	-	33.4	29.29	27.07	-	-	-
SwinIR-MetaSR [■]	38.26	34.77	32.47	29.09	27.02	24.82	34.14	30.66	28.85	26.58	25.09	23.33	32.39	29.31	27.75	25.94	24.86	23.59	33.29	29.12	26.76	24.16	22.75	21.31
SwinIR-LIIF [■]	38.28	34.87	32.73	29.25	27.36	24.99	34.14	30.75	28.98	26.52	25.34	23.39	32.39	29.34	27.84	26.07	25.01	23.64	33.36	29.33	27.15	24.59	23.14	21.43
SwinIR-LTE [■]	38.33	34.89	32.81	29.50	27.35	25.07	34.25	30.80	29.06	26.86	25.42	23.44	32.34	29.39	27.86	26.09	25.03	23.66	33.50	29.41	27.24	24.62	23.17	21.50
SwinIR-LIWT(ours) [■]	38.37	34.94	32.84	29.60	27.51	25.07	34.31	30.86	29.05	26.90	25.43	23.48	32.43	29.39	27.88	26.13	25.06	23.69	33.52	29.46	27.30	24.71	23.24	21.57

Table 2: Quantitative comparison on the benchmark datasets, with the best and second best results highlighted in red and blue, respectively.

4.2 Comparison with Previous Methods

We compare the proposed LIWT with existing arbitrary-scale SR methods [■, ■, ■, ■, ■, ■]. Table 1 presents the PSNR metric results of all comparing methods on the DIV2K validation dataset. As shown in Table 1, our LIWT achieves the best performance across different scaling factors, which indicates that our method can be integrated with different encoders to improve performance. Table 2 depicts the results of LIWT on the four benchmark datasets. Our LIWT achieves the best performance across scaling factors of $\times 6$, $\times 8$, and $\times 12$. At low scaling factors of $\times 2$, $\times 3$, and $\times 4$, our method also achieves the performance in most scenarios. We have also provided a quantitative comparison under non-integer scaling factors in the appendix. Figure 4 shows the visual results of different methods. Benefiting from the high-frequency prior introduced by wavelet transform in the attention mechanism and the curriculum learning strategy, our method achieves accurate structural restoration.



Figure 4: Visual comparison of MetaSR [■], LIIF [■], LTE [■], and LIWT using RDN [■] as the encoder. Zoom in for best view.

Model	DIV2K						B100							
	F^L	F^H	WHFERB	WERB	$\times 2$	$\times 3$	$\times 4$	$\times 6$	$\times 8$	$\times 2$	$\times 3$	$\times 4$	$\times 6$	$\times 8$
✓	✓				34.76	31.09	29.13	26.89	25.53	32.20	29.15	27.65	25.92	24.87
	✓				34.77	31.11	29.14	26.90	25.54	32.22	29.16	27.65	25.92	24.87
✓		✓			34.78	31.11	29.14	26.91	25.54	32.22	29.17	27.67	25.93	24.88
✓	✓				34.79	31.12	29.15	26.91	25.54	32.22	29.16	27.66	25.93	24.87
✓	✓	✓			34.79	31.12	29.15	26.91	25.55	32.23	29.17	27.67	25.93	24.88

Table 3: Ablation study of WERM on the DIV2K validation datasets [■] and B100 [■]. The best performing results are indicated in bold.

4.3 Ablation Study

Effectiveness of WERM. We conduct extensive experiments using EDSR as the encoder to evaluate the effectiveness of WERM, as shown in Table 3. Upon separately removing the branches for processing F^H and F^L , we observe a decrease in performance, indicating the impact of different frequency bands on reconstruction. Similarly, performance degradation is observed upon removing WERM and WHFERB. Figure 5(a) visualizes the features at various stages of WERM. The output F_W of WERM significantly enhances the representation of sharp edge textures (petal edges), with clear distinctions between edge and smooth regions, achieving more prominent discriminability than any feature at previous stages.

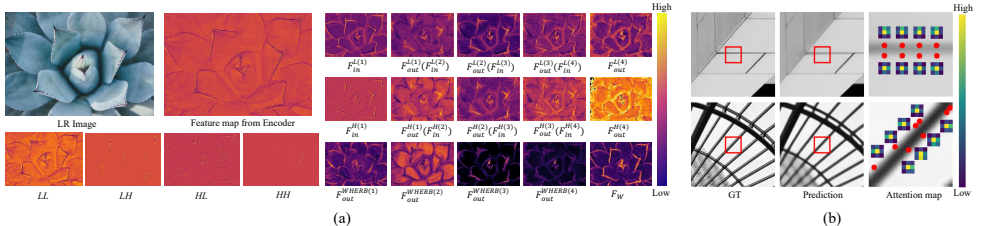


Figure 5: (a) Visualization of feature maps for each stage of WERM; (b) Attention map visualization for WIA.

Methods	Set14					Urban100				
	$\times 2$	$\times 3$	$\times 4$	$\times 6$	$\times 8$	$\times 2$	$\times 3$	$\times 4$	$\times 6$	$\times 8$
LIWT	33.73	30.48	28.75	26.59	25.10	32.44	28.51	26.44	24.08	22.71
LIWT(w/o WMPF)	33.77	30.45	28.73	26.58	25.08	32.45	28.51	26.44	24.03	22.68

Table 4: Ablation study of WMPF on Set14 [31] and Urban100 [24]. The best performing results are indicated in **bold**.

Methods	DIV2K					Urban100				
	$\times 2$	$\times 3$	$\times 4$	$\times 6$	$\times 8$	$\times 2$	$\times 3$	$\times 4$	$\times 6$	$\times 8$
LIWT	34.79	31.12	29.15	26.91	25.55	32.44	28.51	26.44	24.08	22.71
LIWT(SA)	34.79	31.11	29.14	26.91	25.55	32.43	28.49	26.45	24.03	22.68
LIWT(WSA)	34.79	31.11	29.15	26.91	25.54	32.42	28.48	26.45	24.05	22.70

Table 5: Ablation study of WIA on the DIV2K validation set [11] and Urban100 [24]. The best performing results are indicated in **bold**.

Methods	$\times 2$	$\times 3$	$\times 4$	$\times 6$	$\times 8$	$\times 12$	$\times 24$	$\times 27$	$\times 30$
	LIWT	34.79	31.12	29.15	26.91	25.55	23.86	21.30	20.92
LIWT(w/o PE)	31.35	28.32	26.69	24.83	23.69	22.27	20.20	19.86	19.60
LIWT(w/o Cell)	34.67	31.06	29.13	26.90	25.55	23.86	21.29	20.90	20.58

Table 6: Ablation study of positional encoding in WIA, and cell in LIWT on the DIV2K validation set [11]. The best performing results are indicated in **bold**.

Effectiveness of WMPF and WIA. We conduct extensive experiments on different datasets to assess the effectiveness of WMPF and WIA. Table 4 demonstrates a performance decrease at most scaling factors after removing WMPF, indicating the role of high-frequency priors introduced by WMPF. To investigate the effectiveness of the cross-attention mechanism in WIA, we design the following two variant networks based on the self-attention mechanism: (1) LIWT(SA): replacing the query q with the latent embedding obtained by projecting the features Z from the encoder; (2) LIWT(WSA): replacing both the query q and key k with the latent embedding obtained by projecting F_W^\uparrow . Table 5 shows that LIWT achieves the best results across various scaling factors except for $\times 4$ on Urban100 only. We provide visualizations of the cross-attention maps in Figure 5(b) to visually illustrate the effectiveness of WIA. The direction of attention map distribution aligns with the direction of these high-frequency details. This indicates that WIA successfully captures sharp-edge detail features. Besides, we observe a performance drop by removing the positional encoding and cell in Table 6, highlighting the importance of position and pixel size information for LIWT.

Complexity analysis. We investigate the computational consumption on an NVIDIA RTX 3090 24GB device. We use LR images of 192×192 size as input and evaluated them in the $\times 4$ SR task. As shown in Table 7, although our model is slightly inferior to LTE [16] and LIIF [8] in terms of model size, memory consumption, and inference time, it can bring a PSNR improvement of more than 0.1 dB.

Method	Eval/Query	Params	Mem(GB)	Time(s)	PSNR
LIIF [5]	96x96	1.57M	2.5	0.28	27.53
LTE [10]	96x96	1.71M	2.5	0.26	27.57
Ours	96x96	3.97M	3.1	0.50	27.68

Table 7: Comparisons of computational consumption of different methods.

5 Conclusion

In this paper, we propose a novel Local Implicit Wavelet Transformer for arbitrary-scale SR. Specifically, we introduce high-frequency prior information of the features via discrete wavelet transform and a Wavelet Enhancement Residual Module and then effectively utilize high-frequency priori information to improve the reconstruction performance by utilizing the proposed Wavelet Mutual Projected Fusion and Wavelet-aware Implicit Attention module. Extensive experiments have shown that LIWT has superior performance to other methods.

A Appendix

A.1 Haar Wavelet Transform

The Haar wavelet transform is a simple and computationally efficient method for decomposing input signals into low-frequency and high-frequency sub-bands, widely employed in the field of computer vision [11, 12, 13, 14, 30, 32]. In this paper, we utilize the Haar wavelet transform to perform the discrete wavelet transform (DWT) on the features Z obtained from the encoder. The Haar wavelet transform typically involves processing the input signal with high-pass filter H^T and low-pass filter L^T to obtain different sub-bands. Specifically, the low-pass and high-pass filters are:

$$\mathbf{L}^T = \frac{1}{\sqrt{2}} \begin{bmatrix} 1 & 1 \end{bmatrix}, \quad \mathbf{H}^T = \frac{1}{\sqrt{2}} \begin{bmatrix} -1 & 1 \end{bmatrix} \quad (7)$$

Similarly, the filters of the Haar wavelet transform consist of four 2×2 kernels, including LL^T , LH^T , HL^T and HH^T . In this paper, we use LL^T to process the feature Z to obtain the low-frequency component LL , and respectively use LH^T , HL^T and HH^T to process the feature Z to obtain the high-frequency components LH , HL and HH . Following the wavelet transform, the low-frequency component exhibits smooth surface and texture information, while the high-frequency components capture more complex texture details. We denote the low-frequency component LL as F^L and concatenate the high-frequency components LH , HL , and HH along the channel axis, represented as F^H .

A.2 Analysis on the training strategy

We analyzed the impact of training strategies on the DIV2K dataset [11]. As shown in Table 8, training within a small scale sampling range of $s \sim U(1, 4)$ enables the model to achieve good performance at small upscaling scales but sacrifices reconstruction accuracy at higher scaling factors. Expanding the scale sampling range to $s \sim U(1, 8)$ during training can enhance the model’s reconstruction performance at larger upscaling scales but decrease performance at smaller upscaling scales. Our proposed curriculum learning strategy gradually expands the sampling range during training. Although the performance at scaling factors of $\times 2$ and $\times 3$ is not as good as training within the small-scale sampling range of $s \sim U(1, 4)$, overall,

it achieves the best balance across different scaling factors. Our training approach ensures effective reconstruction at large sampling scales and achieves the most optimal or suboptimal results across various scaling factors. To validate the generality of the proposed curriculum learning training strategy, we applied the same training setup to LIIF [5] and LTE [16]. As shown in Table 9, we observed performance improvements, indicating the effectiveness and generalizability of our training strategy.

Training strategy	$\times 2$	$\times 3$	$\times 4$	$\times 6$	$\times 8$	$\times 12$	$\times 24$	$\times 27$	$\times 30$
Curriculum learning strategy	34.79	31.12	29.15	26.91	25.55	23.86	21.3	20.92	20.6
Training with $U(1, 4)$	34.84	31.13	29.14	26.89	25.52	23.83	21.27	20.89	20.57
Training with $U(1, 8)$	34.78	31.11	29.14	26.91	25.55	23.86	21.31	20.92	20.6

Table 8: The average PSNR (dB) of different training strategies on the DIV2K validation set [3].

Training strategy	Method	$\times 2$	$\times 3$	$\times 4$	$\times 6$	$\times 12$	$\times 18$
		EDSR-LIIF [5]	34.67	30.96	29	26.75	23.71
Original	EDSR-LTE [16]	34.72	31.02	29.04	26.81	23.78	22.23
	EDSR-LTE [16]	34.72	31.02	29.04	26.81	23.78	22.23
Curriculum	EDSR-LIIF [5]	34.65(-0.02)	30.99(+0.03)	29.05(+0.05)	26.81(+0.06)	23.77(+0.06)	22.22(+0.05)
	EDSR-LTE [16]	34.7(-0.02)	31.03(+0.01)	29.07(+0.03)	26.85(+0.04)	23.82(+0.04)	22.28(+0.05)

Table 9: The average PSNR (dB) of LIIF [5] and LTE [16] training with and without curriculum learning on the DIV2K validation set [3].

A.3 More evaluation metrics

We employ two metrics, SSIM and LPIPS, to further demonstrate the effectiveness of LIWT compared to other arbitrary-scale SR methods. We compare the performance of LIWT, LTE [16], LIIF [5], and MetaSR [31] using SwinIR as the encoder on Set14 [31] and Urban100 [24] datasets. Typically, higher SSIM and lower LPIPS correspond to better performance. From the results in Table 10, it can be observed that except for $\times 2$ scaling, our method achieves the highest SSIM and the lowest LPIPS. This indicates that our approach can recover more structural information and has better perceptual quality.

Dataset	Method	$\times 2$		$\times 3$		$\times 4$		$\times 6$		$\times 8$	
		SSIM \uparrow	LPIPS \downarrow								
Set14 [31]	Meta-SR [31]	0.923	0.134	0.850	0.227	0.791	0.291	0.704	0.382	0.648	0.446
	LIIF [5]	0.923	0.134	0.851	0.227	0.792	0.293	0.707	0.380	0.652	0.443
	LTE [16]	0.924	0.133	0.852	0.224	0.794	0.292	0.709	0.377	0.655	0.440
	LIWT(Ours)	0.924	0.132	0.853	0.223	0.795	0.289	0.712	0.373	0.657	0.436
Urban100 [24]	Meta-SR [31]	0.939	0.102	0.873	0.186	0.810	0.251	0.709	0.347	0.638	0.415
	LIIF [5]	0.939	0.102	0.876	0.188	0.817	0.258	0.719	0.349	0.650	0.415
	LTE [16]	0.941	0.100	0.877	0.186	0.820	0.254	0.722	0.343	0.653	0.408
	LIWT(Ours)	0.941	0.099	0.878	0.183	0.821	0.250	0.726	0.336	0.657	0.401

Table 10: Comparison of more evaluation metrics (SSIM \uparrow and LPIPS \downarrow) on Set14 [31] and Urban100 [24].

A.4 Comparison with DWT-based SR methods

We compare LIWT with other DWT-based SR methods [1, 2, 3, 28, 30, 32] using PSNR and SSIM metrics on Set14 [31] and Urban100 [24], where LIWT utilizes SwinIR [31] as the encoder. As shown in Table 11, our LIWT achieves the best results at various scaling factors.

Dataset	Method	x2		x3		x4	
		PSNR↑	SSIM↑	PSNR↑	SSIM↑	PSNR↑	SSIM↑
Set14 [51]	MWCNN [52]	33.71	0.918	30.14	0.841	28.58	0.788
	DWSR [53]	33.07	0.911	29.83	0.831	28.04	0.767
	WRAN [54]	34.21	0.922	30.71	0.852	28.60	0.786
	WDRN [55]	33.90	0.921	30.50	0.845	28.75	0.786
	JWSGN [56]	34.17	0.923	-	-	28.96	0.789
	WaveMixSR [57]	31.27	0.904	28.77	0.841	26.25	0.751
Urban100 [52]	LIWT(Ours)	34.31	0.924	30.86	0.853	29.05	0.795
	MWCNN [52]	32.36	0.931	28.19	0.852	26.37	0.789
	DWSR [53]	30.46	0.916	-	-	25.26	0.755
	WRAN [54]	33.47	0.940	28.99	0.869	26.74	0.803
	WDRN [55]	32.64	0.937	28.59	0.862	26.41	0.797
	JWSGN [56]	33.17	0.938	-	-	26.82	0.807
Urban100 [52]	WaveMixSR [57]	29.14	0.908	25.82	0.819	23.57	0.730
	LIWT(Ours)	33.52	0.941	29.46	0.878	27.30	0.821

Table 11: Comparison of PSNR↑ and SSIM↑ for different DWT-based methods on Set14 [51] and Urban100 [52].

A.5 Comparison of different arbitrary-scale SR methods at non-integer scale

To further assess the advantages of our method over other arbitrary-scale SR methods, we present comparative results of PSNR and SSIM metrics at non-integer scaling factors on Set14 [51] and Urban100 [52]. As shown in Table 12, Our LIWT achieves optimal results at various scaling factors.

Dataset	Method	x2.2		x2.5		x3.3		x3.5		x4.4		x5.5		x6.6		x7.7	
		PSNR↑	SSIM↑														
Set14 [51]	Meta-SR [58]	31.84	0.899	31.48	0.883	29.14	0.825	29.26	0.813	28.18	0.766	26.92	0.720	26.14	0.684	25.32	0.654
	LIIF [59]	31.91	0.899	31.54	0.884	29.44	0.825	29.29	0.814	28.25	0.770	27.02	0.722	26.25	0.688	25.41	0.658
	LTE [59]	31.92	0.900	31.55	0.884	29.48	0.826	29.30	0.815	28.29	0.771	27.07	0.724	26.30	0.689	25.50	0.661
	LIWT(Ours)	31.95	0.900	31.60	0.885	29.49	0.827	29.34	0.816	28.31	0.772	27.08	0.725	26.33	0.691	25.50	0.662
Urban100 [52]	Meta-SR [58]	31.92	0.923	28.37	0.887	29.07	0.851	27.73	0.824	26.56	0.785	24.17	0.701	23.01	0.684	22.45	0.645
	LIIF [59]	31.78	0.924	28.48	0.885	28.26	0.854	27.67	0.840	26.24	0.792	24.96	0.739	23.97	0.694	23.18	0.656
	LTE [59]	31.92	0.925	28.51	0.887	28.38	0.856	27.76	0.842	26.33	0.796	25.04	0.742	24.04	0.698	23.21	0.659
	LIWT(Ours)	31.95	0.925	28.51	0.886	28.41	0.857	27.81	0.843	26.39	0.797	25.13	0.746	24.12	0.701	23.29	0.662

Table 12: Comparison of different arbitrary-scale SR methods at non-integer scale on Set14 [51] and Urban100 [52] (PSNR (dB)).

A.6 The analysis of large-scale SR

We analyzed the advantages of our LIWT on the benchmark dataset for large-scale SR scenarios. We define scales larger than $\times 6$ as large-scale. As shown in Table 13, our method achieves optimal results for large-scale at $\times 6$, $\times 8$, and $\times 12$. As shown in Figure 6, LIWT with RDN [53] as the encoder can even outperform other methods with SwinIR [50] as the encoder at $\times 8$ SR on Set5 [2].

Methods	Set5 [50]			Set14 [51]			B100 [52]			Urban100 [52]		
	$\times 6$	$\times 8$	$\times 12$	$\times 6$	$\times 8$	$\times 12$	$\times 6$	$\times 8$	$\times 12$	$\times 6$	$\times 8$	$\times 12$
RDN-Meta-SR [53]	29.04	26.96	-	26.51	24.97	-	25.90	24.83	-	23.99	22.59	-
RDN-LIIF [59]	29.15	27.14	24.86	26.64	25.15	23.24	25.98	24.91	23.57	24.20	22.79	21.15
RDN-UltraSR [59]	29.33	27.24	24.81	26.69	25.25	23.32	26.01	24.96	23.59	24.30	22.87	21.20
RDN-IPE [59]	29.25	27.22	-	26.58	25.09	-	26.00	24.93	-	24.26	22.87	-
RDN-LTE [59]	29.32	27.26	24.79	26.71	25.16	23.31	26.01	24.95	23.6	24.28	22.88	21.22
RDN-LIWT (Ours)	29.45	27.38	25.00	26.80	25.30	23.36	26.05	24.99	23.63	24.41	23.01	21.33
SwinIR-Meta-SR [50]	29.09	27.02	24.82	26.58	25.09	23.33	25.94	24.86	23.59	24.16	22.75	21.31
SwinIR-LIIF [59]	29.46	27.36	24.99	26.82	25.34	23.39	26.07	25.01	23.64	24.59	23.14	21.43
SwinIR-LTE [59]	29.50	27.35	25.07	26.86	25.42	23.44	26.09	25.03	23.66	24.62	23.17	21.50
SwinIR-LIWT (Ours)	29.60	27.51	25.07	26.90	25.43	23.48	26.13	25.06	23.69	24.71	23.24	21.57

Table 13: Comparison for scales at $\times 2$, $\times 3$, and $\times 4$ on benchmark datasets (PSNR (dB)).

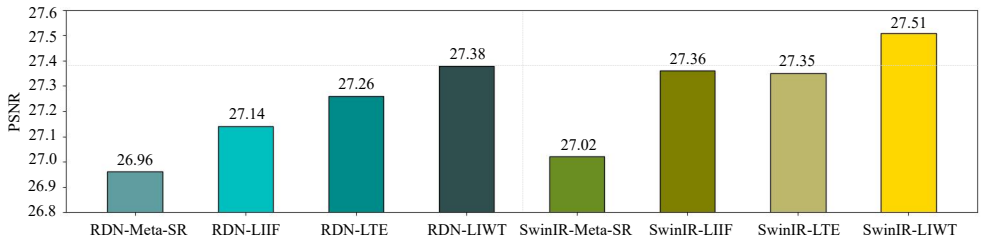


Figure 6: Comparison of $\times 8$ SR task on Set5 [2] (PSNR (dB)).

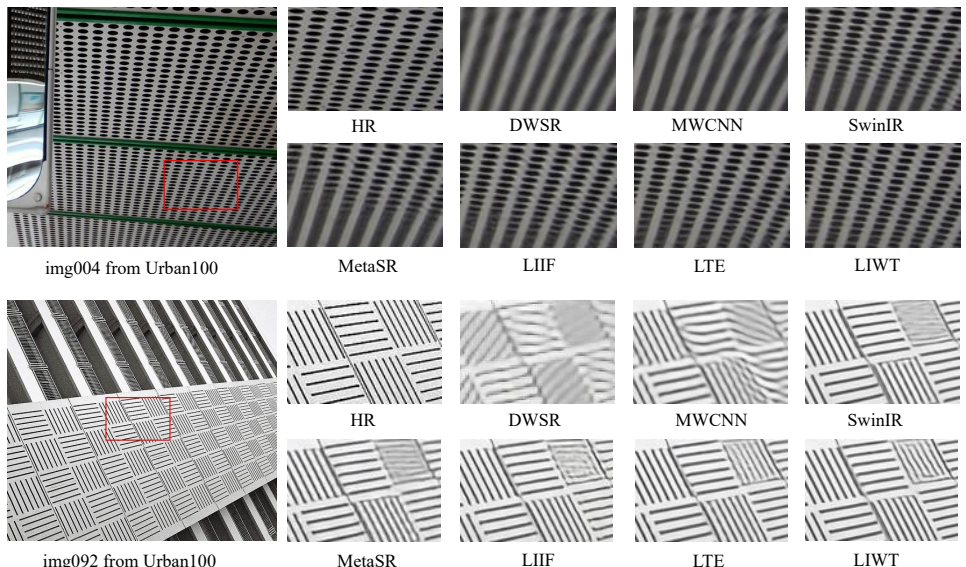


Figure 7: Visual comparisons for $\times 4$ SR on Urban100 [14]. Zoom in for best view.

References

- [1] Eirikur Agustsson and Radu Timofte. Ntire 2017 challenge on single image super-resolution: Dataset and study. In *Proceedings of the IEEE conference on computer vision and pattern recognition workshops*, pages 126–135, 2017.
- [2] Marco Bevilacqua, Aline Roumy, Christine Guillemot, and Marie Line Alberi-Morel. Low-complexity single-image super-resolution based on nonnegative neighbor embedding. 2012.
- [3] Hanting Chen, Yunhe Wang, Tianyu Guo, Chang Xu, Yiping Deng, Zhenhua Liu, Siwei Ma, Chunjing Xu, Chao Xu, and Wen Gao. Pre-trained image processing transformer. In *Proceedings of the IEEE/CVF conference on computer vision and pattern recognition*, pages 12299–12310, 2021.
- [4] Hao-Wei Chen, Yu-Syuan Xu, Min-Fong Hong, Yi-Min Tsai, Hsien-Kai Kuo, and Chun-Yi Lee. Cascaded local implicit transformer for arbitrary-scale super-resolution.

In *Proceedings of the IEEE/CVF Conference on Computer Vision and Pattern Recognition*, pages 18257–18267, 2023.

- [5] Yinbo Chen, Sifei Liu, and Xiaolong Wang. Learning continuous image representation with local implicit image function. In *Proceedings of the IEEE/CVF conference on computer vision and pattern recognition*, pages 8628–8638, 2021.
- [6] Tao Dai, Jianrui Cai, Yongbing Zhang, Shu-Tao Xia, and Lei Zhang. Second-order attention network for single image super-resolution. In *Proceedings of the IEEE/CVF conference on computer vision and pattern recognition*, pages 11065–11074, 2019.
- [7] Chao Dong, Chen Change Loy, Kaiming He, and Xiaoou Tang. Image super-resolution using deep convolutional networks. *IEEE transactions on pattern analysis and machine intelligence*, 38(2):295–307, 2015.
- [8] Chao Dong, Chen Change Loy, and Xiaoou Tang. Accelerating the super-resolution convolutional neural network. In *Computer Vision–ECCV 2016: 14th European Conference, Amsterdam, The Netherlands, October 11–14, 2016, Proceedings, Part II 14*, pages 391–407. Springer, 2016.
- [9] Minghong Duan, Linhao Qu, Zhiwei Yang, Manning Wang, Chenxi Zhang, and Zhi-jian Song. Towards arbitrary-scale histopathology image super-resolution: An efficient dual-branch framework via implicit self-texture enhancement. *arXiv preprint arXiv:2401.15613*, 2024.
- [10] Bahadir K Gunturk, Yucel Altunbasak, and Russell M Mersereau. Super-resolution reconstruction of compressed video using transform-domain statistics. *IEEE Transactions on Image Processing*, 13(1):33–43, 2004.
- [11] Tiantong Guo, Hojjat Seyed Mousavi, Tiep Huu Vu, and Vishal Monga. Deep wavelet prediction for image super-resolution. In *Proceedings of the IEEE conference on computer vision and pattern recognition workshops*, pages 104–113, 2017.
- [12] Wei-Yen Hsu and Pei-Wen Jian. Wavelet detail perception network for single image super-resolution. *Pattern Recognition Letters*, 166:16–23, 2023.
- [13] Xuecai Hu, Haoyuan Mu, Xiangyu Zhang, Zilei Wang, Tieniu Tan, and Jian Sun. Meta-sr: A magnification-arbitrary network for super-resolution. In *Proceedings of the IEEE/CVF conference on computer vision and pattern recognition*, pages 1575–1584, 2019.
- [14] Jia-Bin Huang, Abhishek Singh, and Narendra Ahuja. Single image super-resolution from transformed self-exemplars. In *Proceedings of the IEEE conference on computer vision and pattern recognition*, pages 5197–5206, 2015.
- [15] Pranav Jeevan, Akella Srinidhi, Pasunuri Prathiba, and Amit Sethi. Wavemixsr: Resource-efficient neural network for image super-resolution. In *Proceedings of the IEEE/CVF Winter Conference on Applications of Computer Vision*, pages 5884–5892, 2024.
- [16] Jaewon Lee and Kyong Hwan Jin. Local texture estimator for implicit representation function. In *Proceedings of the IEEE/CVF conference on computer vision and pattern recognition*, pages 1929–1938, 2022.

- [17] Jingyun Liang, Jiezhang Cao, Guolei Sun, Kai Zhang, Luc Van Gool, and Radu Timofte. Swinir: Image restoration using swin transformer. In *Proceedings of the IEEE/CVF international conference on computer vision*, pages 1833–1844, 2021.
- [18] Bee Lim, Sanghyun Son, Heewon Kim, Seungjun Nah, and Kyoung Mu Lee. Enhanced deep residual networks for single image super-resolution. In *Proceedings of the IEEE conference on computer vision and pattern recognition workshops*, pages 136–144, 2017.
- [19] Pengju Liu, Hongzhi Zhang, Wei Lian, and Wangmeng Zuo. Multi-level wavelet convolutional neural networks. *IEEE Access*, 7:74973–74985, 2019.
- [20] Ying-Tian Liu, Yuan-Chen Guo, and Song-Hai Zhang. Enhancing multi-scale implicit learning in image super-resolution with integrated positional encoding. *arXiv preprint arXiv:2112.05756*, 2021.
- [21] David Martin, Charless Fowlkes, Doron Tal, and Jitendra Malik. A database of human segmented natural images and its application to evaluating segmentation algorithms and measuring ecological statistics. In *Proceedings Eighth IEEE International Conference on Computer Vision. ICCV 2001*, volume 2, pages 416–423. IEEE, 2001.
- [22] Yiqun Mei, Yuchen Fan, and Yuqian Zhou. Image super-resolution with non-local sparse attention. In *Proceedings of the IEEE/CVF conference on computer vision and pattern recognition*, pages 3517–3526, 2021.
- [23] Ben Niu, Weilei Wen, Wenqi Ren, Xiangde Zhang, Lianping Yang, Shuzhen Wang, Kaihao Zhang, Xiaochun Cao, and Haifeng Shen. Single image super-resolution via a holistic attention network. In *Computer Vision–ECCV 2020: 16th European Conference, Glasgow, UK, August 23–28, 2020, Proceedings, Part XII 16*, pages 191–207. Springer, 2020.
- [24] Wenzhe Shi, Jose Caballero, Christian Ledig, Xiahai Zhuang, Wenjia Bai, Kanwal Bhatia, Antonio M Simoes Monteiro de Marvao, Tim Dawes, Declan O'Regan, and Daniel Rueckert. Cardiac image super-resolution with global correspondence using multi-atlas patchmatch. In *Medical Image Computing and Computer-Assisted Intervention–MICCAI 2013: 16th International Conference, Nagoya, Japan, September 22–26, 2013, Proceedings, Part III 16*, pages 9–16. Springer, 2013.
- [25] Wenzhe Shi, Jose Caballero, Ferenc Huszár, Johannes Totz, Andrew P Aitken, Rob Bishop, Daniel Rueckert, and Zehan Wang. Real-time single image and video super-resolution using an efficient sub-pixel convolutional neural network. In *Proceedings of the IEEE conference on computer vision and pattern recognition*, pages 1874–1883, 2016.
- [26] Matt W Thornton, Peter M Atkinson, and DA Holland. Sub-pixel mapping of rural land cover objects from fine spatial resolution satellite sensor imagery using super-resolution pixel-swapping. *International Journal of Remote Sensing*, 27(3):473–491, 2006.
- [27] Bin Xia, Yucheng Hang, Yapeng Tian, Wenming Yang, Qingmin Liao, and Jie Zhou. Efficient non-local contrastive attention for image super-resolution. In *Proceedings of the AAAI conference on artificial intelligence*, volume 36, pages 2759–2767, 2022.

- [28] Jingwei Xin, Jie Li, Xinrui Jiang, Nannan Wang, Heng Huang, and Xinbo Gao. Wavelet-based dual recursive network for image super-resolution. *IEEE Transactions on Neural Networks and Learning Systems*, 33(2):707–720, 2020.
- [29] Xingqian Xu, Zhangyang Wang, and Humphrey Shi. Ultrasr: Spatial encoding is a missing key for implicit image function-based arbitrary-scale super-resolution. *arXiv preprint arXiv:2103.12716*, 2021.
- [30] Shengke Xue, Wenyuan Qiu, Fan Liu, and Xinyu Jin. Wavelet-based residual attention network for image super-resolution. *Neurocomputing*, 382:116–126, 2020.
- [31] Roman Zeyde, Michael Elad, and Matan Protter. On single image scale-up using sparse-representations. In *Curves and Surfaces: 7th International Conference, Avignon, France, June 24-30, 2010, Revised Selected Papers 7*, pages 711–730. Springer, 2012.
- [32] Yulun Zhang, Kunpeng Li, Kai Li, Lichen Wang, Bineng Zhong, and Yun Fu. Image super-resolution using very deep residual channel attention networks. In *Proceedings of the European conference on computer vision (ECCV)*, pages 286–301, 2018.
- [33] Yulun Zhang, Yapeng Tian, Yu Kong, Bineng Zhong, and Yun Fu. Residual dense network for image super-resolution. In *Proceedings of the IEEE conference on computer vision and pattern recognition*, pages 2472–2481, 2018.
- [34] Wenbin Zou, Liang Chen, Yi Wu, Yunchen Zhang, Yuxiang Xu, and Jun Shao. Joint wavelet sub-bands guided network for single image super-resolution. *IEEE Transactions on Multimedia*, 2022.
- [35] Wilman WW Zou and Pong C Yuen. Very low resolution face recognition problem. *IEEE Transactions on image processing*, 21(1):327–340, 2011.